Development of low-scatter optical edges for starshades

John Steeves, Hyeong Jae Lee, Evan Hilgemann, David Webb, Stuart Shaklan, Stefan Martin, Douglas Lisman, Dylan McKeithen, Christine Bradley

Jet Propulsion Laboratory, California Institute of Technology, 4800 Oak Grove Dr, Pasadena, CA, USA 91109

ABSTRACT

Starshades, combined with future space telescopes, provide the ability to detect Earth-like exoplanets in the habitable zone by producing high contrast ratios at small inner working angles. The primary function of a starshade is to suppress light from a target star such that its orbiting planets are revealed. In order to do so, the optical edges of the starshade must maintain their precise in-plane profile to produce the necessary apodization function. However, an equally important consideration is the interaction of these edges with light emanating from our own Sun as scattered and/or diffracted sunlight can significantly degrade the achievable contrast. This paper describes the technical efforts performed to obtain precision, low-scatter optical edges for future starshades. Trades between edge radius (i.e. sharpness) and surface reflectivity have been made and small-scale coupons have been produced using scalable manufacturing processes. A custom scattered light testbed has been developed to quantify the magnitude of scattered light over all sun angles. Models have also been developed to make predictions on the level of reflected and/or diffracted light for various edge architectures. The results of these studies have established a current baseline approach which implements photochemical etching techniques on thin metal foils.

Keywords: Starshades, optical edges, scatter, diffraction, high contrast imaging

1. INTRODUCTION

The detection and characterization of Earth-like exoplanets around Sun-like stars was recognized as a top priority by the NASA Astrophysics 30-year roadmap.[1] Starshades, combined with future space telescopes offer the ability to detect such planets by providing high levels of starlight suppression (10^{10}) at small inner working angles ($<$ 100 mas). Several exoplanet-detecting mission studies incorporating starshades have been conducted or are currently under study including the Habitable Exoplanet Imaging Mission (HabEx) concept,[2] a rendezvous with the WFIRST telescope,[3] and the Exo-S Probe.[4] While the detailed requirements on the starshades vary between these studies, the underlying challenges remain constant. In particular the starshade must deploy to its characteristic flower-like shape, shown in Figure 1, and maintain this shape throughout the lifetime of the mission. This is necessary to achieve the proper apodization function required to produce the desired level of starlight suppression. This apodization function is ultimately defined by the terminal portions of the petals, known as the optical edges. The in-plane profile of the optical edges must be held to sub-millimeter precision levels over the entire starshade perimeter otherwise unwanted starlight will leak through and overwhelm the signal from the orbiting planet.

The interaction of the starshade with light emanating from the sun is also of great importance. By ensuring that the sun remains on the "star side" of the starshade, and by designing the structure to be sufficiently slender in profile, sunlight can only scatter towards the telescope off of the optical edges. This interaction can be through reflection, diffraction, or a combination of both depending on the relative angle of the starshade with respect to the sun. Therefore, it is essential to develop optical edges that reduce the total amount of scattered sunlight entering the telescope over all possible sun angles. For current mission concepts, such as the Starshade rendezvous mission with WFIRST, sun angles between 40° and 85°, measured with respect to the axis defined by the telescope/starshade/star line of sight, are of relevance.

For further information contact John Steeves: john.b.steeves@jpl.nasa.gov

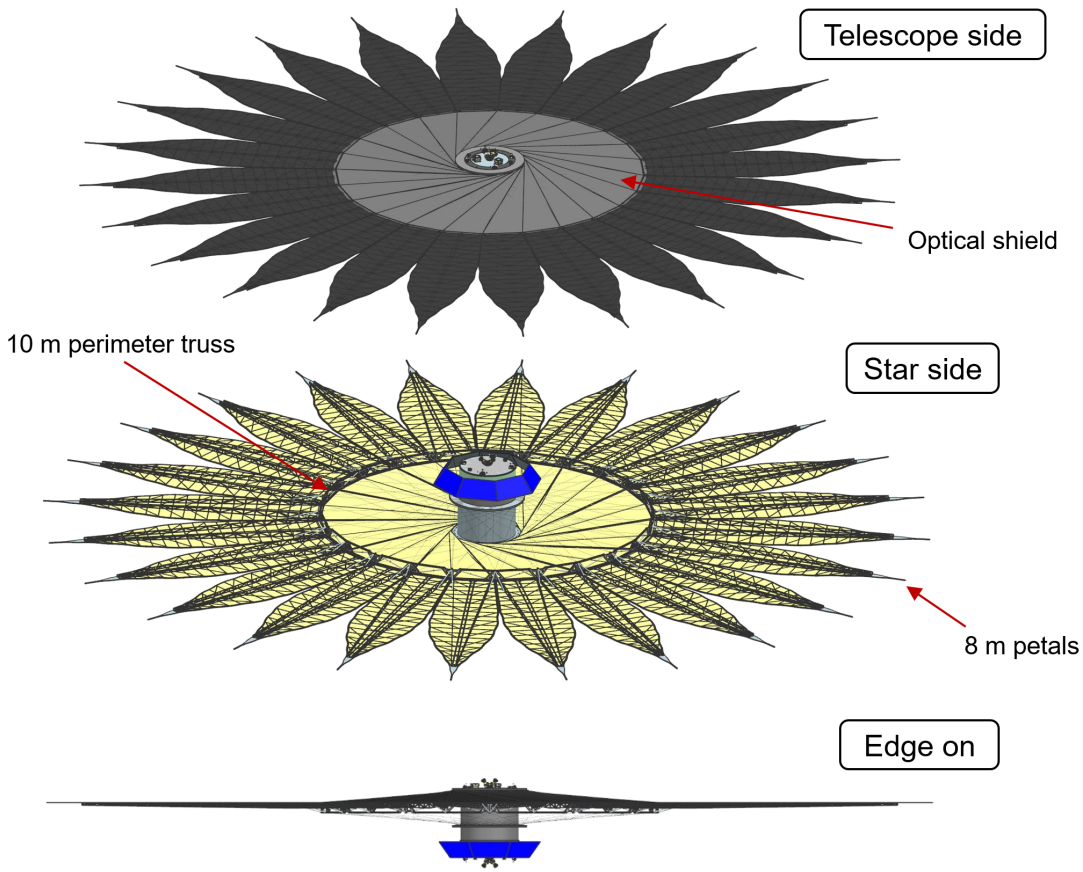

Figure 1. Deployed starshade displaying the various subsystems.

This paper describes the technical efforts performed to date to develop precision low-scatter optical edges for future starshades. Section 2 provides an overview of the optical edge design including techniques to achieve the required in-plane profile and sharp beveled edge, along with experiments incorporating anti-reflective coatings. Section 3 describes the scatterometer testbed developed to assess the scattered-light performance of various optical edge coupons. A geometrical scatter model used to make predictions on the scattered light performance is presented in Section 4. Section 5 describes a method to decrease the overall scattered light using a technique known as "stealth edges". Finally, Section 6 discusses the results and concludes the paper.

2. OPTICAL EDGE DESIGN

A detailed view of a starshade petal is shown in Figure 2 with the various structural components highlighted for clarity. In the deployed state, the petal must maintain its in-plane profile to sub-millimeter precision levels.[5] This presents challenges in both the manufacturing processes and on-orbit stability requirements. To ease manufacturing and assembly, meter-scale optical edge segments are constructed independently and then integrated onto the continuous structural edge. Therefore simplified individual segments can be manufactured to tight tolerances and then precision bonded onto the full-scale petal. In doing so, the mechanical requirements of the full petal shift from dimensional precision (i.e. during manufacture) to dimensional stability (i.e. during operation). In particular, stability over a wide range of temperature regimes is achieved through the use of low-CTE materials, namely carbon fiber composites.

A cross-section of the petal edge is shown in Figure 3. The optical edge assembly is comprised of a carbon-fiber reinforced polymer (CFRP) substrate bonded to the top surface of the low-scatter optical edge film. Note that the figure is not to scale, as the optical edge foil is only 0.38 mm thick. Due to the low thickness of the

foil, the CFRP substrate is necessary to mechanically support the optical edge such that it can be aligned and bonded to the continuous structural edge of the petal. The CFRP substrate and structural edge are made from the same material and have the same thickness such that the approximate neutral axis of the entire stack up coincides with the optical edge foil. This is essential for reasons including thermal balancing and strain in the stowed configuration (see Ref. [6 and 7] for the details of this process).

Two views are shown in Figure 3 that correspond to the "trailing edge" and "leading edge" conditions, depending on the relative position and orientation of the starshade petal with respect to the sun. In the trailing edge condition, the relative distance between the CFRP substrate and the optical edge, D_1, is of importance. This distance is chosen such that the CFRP substrate shades the optical edge over all sun angles, ensuring that there is no direct path for sunlight to reach the terminal portion of the optical edge. For the leading edge condition, the relative set-back between the structural edge and the optical edge, D_2, becomes relevant. This distance is chosen such that the light path from the sun does not come in contact with the structural edge, especially at high sun angles. For current starshade designs, sun angles between 40 and 85 degrees are of relevance. Assuming the CFRP substrate and structural edge are approximately 1 mm thick, this results in $D_1 \leq 0.84$ mm and $D_2 \geq 11.5$ mm.

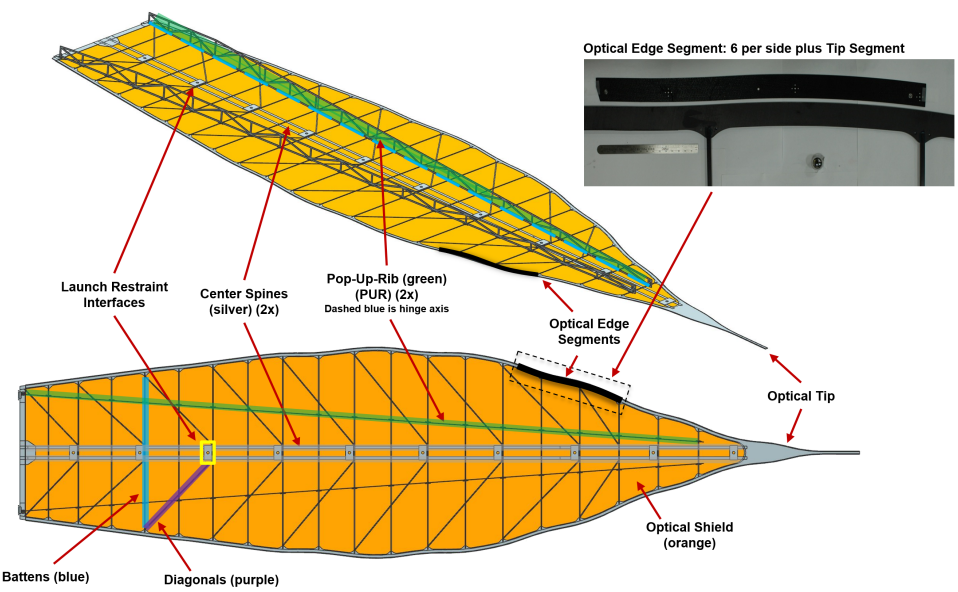

Figure 2. Overview of starshade petal components along with a picture of a 1.0 m long optical edge segment.

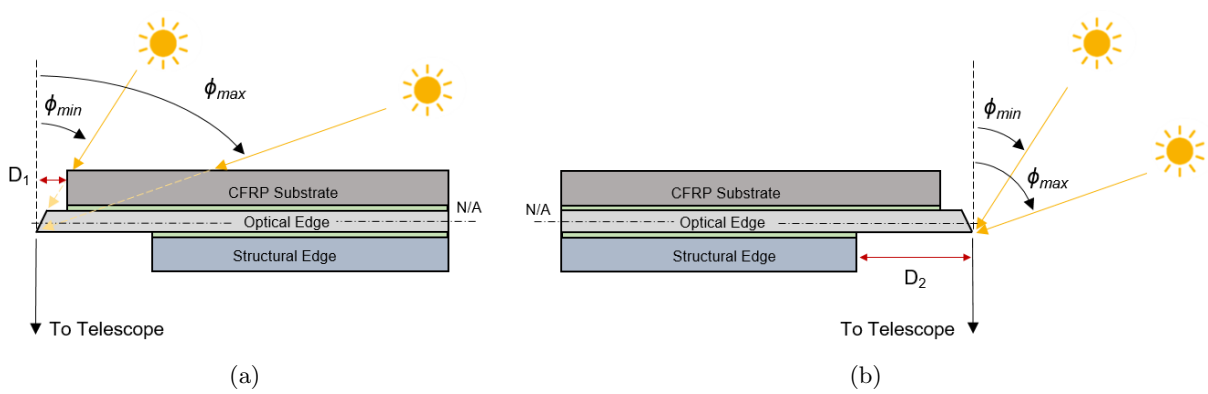

(a) (b)

Figure 3. Optical edge cross section (not to scale) showing a) trailing edge, and b) leading edge conditions and relevant sun angles.

2.1 In-Plane Profile

Chemical etching and photolithographic patterning are used to manufacture the optical edges as these techniques can produce precise in-plane profiles (see Ref [8] for the details of this process). However, early efforts indicated that it was difficult to produce free-standing optical edge foils with the necessary in-plane accuracy. This was attributed to a number of factors including the extremely low bending thickness of the material and the release of internal stresses during the etching process. Several techniques were explored to support the optical edge films during etching; however, many of these resulted in unacceptably complicated manufacturing processes.[8] Therefore, a method to provide mechanical constraint without modifications to the standard etching practices was devised. In this process a simple slot with the desired in-plane profile is etched into a full-width amorphous metal sheet. The terminal edges of this slot are left attached to the remaining material. This optical edge now has support within the plane due to the full-width of the sheet, as opposed to the narrow section associated with previous free-standing prototypes. A picture of a half-scale (0.5 m) prototype constructed in this fashion is shown in Figure 4. Once this slot has been etched, a stiff CFRP substrate can be bonded to the top of the metal film and the excess material removed.

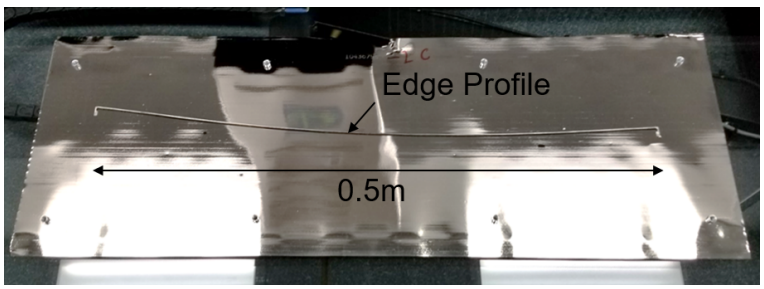

Figure 4. Half-scale optical edge prototype displaying the slotted edge profile produced through photochemical etching techniques.

In order to assess the accuracy of this process, a MicroVu Excel 1051 measurement system, shown in Figure 5, was used to measure the in-plane profile of the optical edge prototypes. The system consists of a downward facing camera mounted on a precision XY gantry. Images are acquired at successive intervals along the length of the prototype and edge-detection algorithms are used to measure the edge profile. Encoders accurate to 0.1 μm allow for each measurement to be stitched together. The system has a 1050 mm $\times$ 1050 mm bed and can thus accommodate full-scale optical edges.

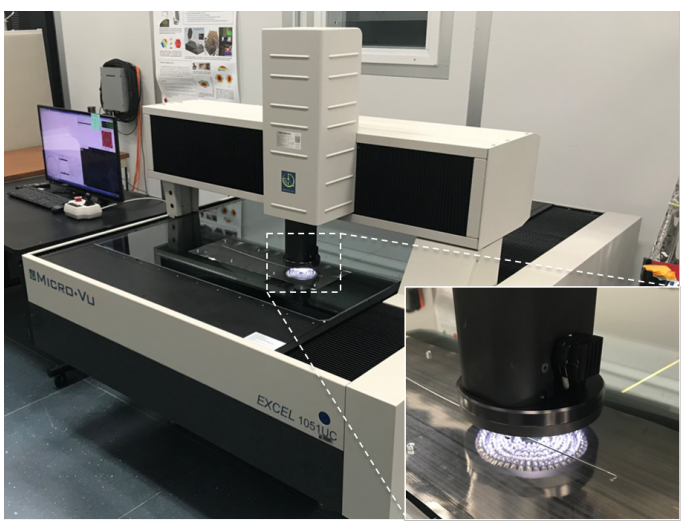

Figure 5. Microvu Excel 1051 measurement system used to measure the in-plane accuracy of optical edge prototypes.

Figure 6 displays the measured in-plane accuracy of three 0.5 m long optical edge profiles. Each prototype was measured twice with the sheet physically removed from the MicroVu scanner in between each measurement. This was performed to assess the effect of manually handling the unsupported optical edge foil. From the measurements it is apparent that the repeatability in this process is relatively high, however some variations are present especially for Sheet A. This is attributed to out-of-plane deformations in the material that are due to the extremely low bending stiffness of the thin sheet. These out-of-plane variations cause the camera in the MicroVu system to lose focus which affects the edge detection algorithms and ultimately the accuracy of the in-plane measurement. On average the error in the in-plane profile is approximately 10-15 μm RMS, and is nearing the requirements for future starshade designs.[5] Further work is underway to better understand these errors and improve upon the manufactured precision.

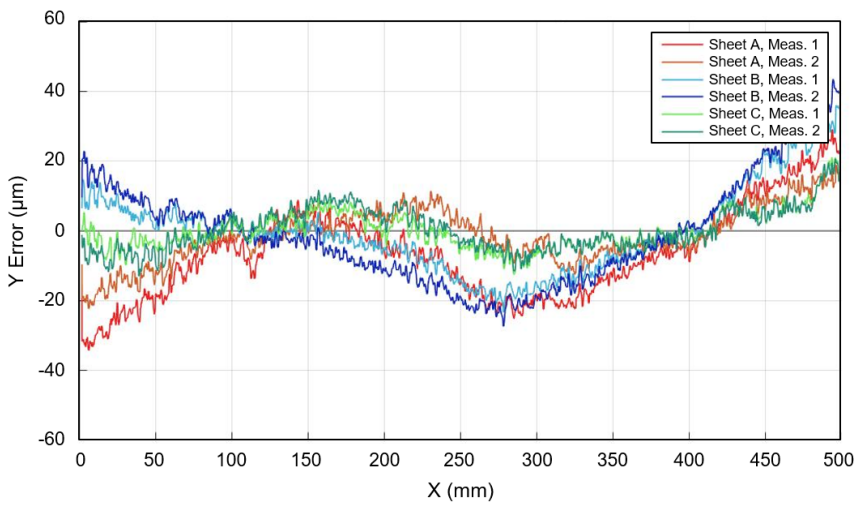

Figure 6. Measured in-plane accuracy of three optical edge prototypes.

2.2 Sharp Terminal Edge

The chemical etching process used to create the in-plane profile also produces the desired bevel through the thickness of the material as well as a sharp terminal edge. This is due to the isotropic nature of the single-sided etching process where material is removed gradually in equipotential lines, leaving a sloped shape as shown in Figure 7(a). In our previous efforts, it was determined that amorphous metal materials produce the sharpest possible edges due to their their lack of grain structure compared to traditional metals.[8] In particular, alloys 2826MB and MBF23 from Metglas have been shown to be the highest performing materials in terms of edge sharpness and regularity. Figure 7(b) displays an edge-on view of one such coupon where the terminal portion of the edge has a radius of < 250 nm across its length.

2.3 Anti-Reflective Coatings

Previous efforts have also studied the effect of coating optical edges with anti-reflective materials to absorb a portion of the incident light.[9] These studies were focused on edges that were produced using more traditional manufacturing methods (i.e. wire electrical discharge machining (EDM)) which resulted in edges with a 15 - 20 μm terminal radius. To provide an independent assessment of these processes, edges of this design were also produced for this study. Figure 8(a) is an SEM image of a titanium edge with a bevel produced through wire EDM. The radius of curvature of the terminal edge is approximately 15 - 20 μm, matching that of Ref [9]. Figures 8(b) and 8(c) are SEM images of coupons that have been coated with Enbio SolarBlack and Acktar Magic Black. It is apparent that the coatings produce a more textured surface on the titanium coupon, which is inherent to the majority of anti-reflective coatings and gives rise to their absorptive properties. The edge sharpness of the coupons is relatively unchanged for both coatings, with terminal radii on the order of 20 μm.

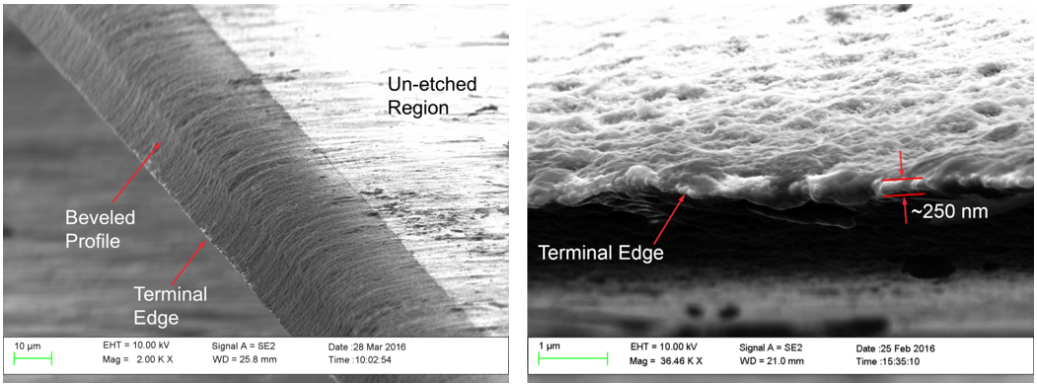

(a) (b)

Figure 7. a) Oblique view and b) edge-on view of an etched amorphous metal coupon.

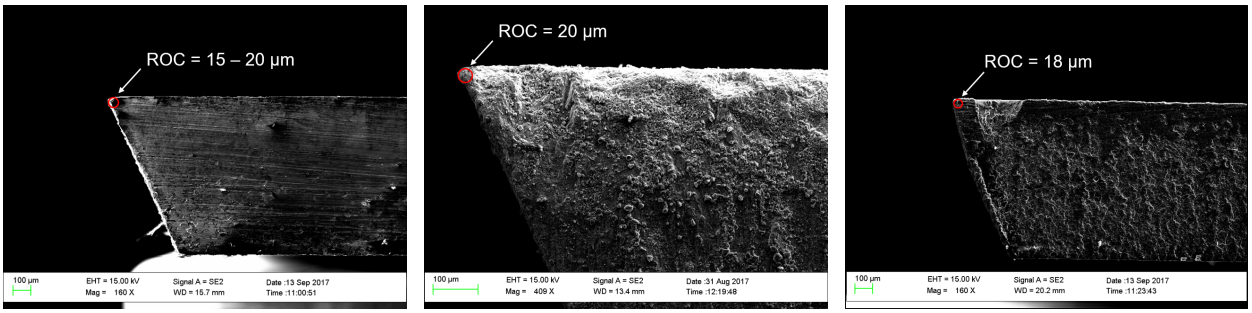

(a) (b) (c)

Figure 8. SEM images of titanium optical edge coupons manufactured through wire-EDM processes with a) no coating, b) Enbio SolarBlack coating, c) Acktar Magic Black coating.

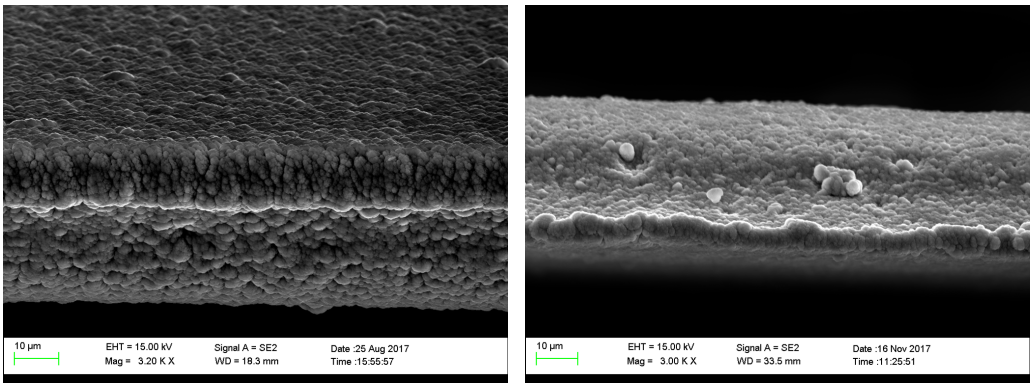

(a) (b)

Figure 9. Edge-on SEM images of etched amorphous metal coupons with Acktar Magic Black coatings in a) standard thickness, and b) reduced-thickness.

Studies were also performed to understand the effect of these coatings on sharp amorphous metal edges. Figure 9 displays SEM images of etched amorphous metal coupons after they were coated with two anti-reflective coatings. The first, Figure 9(a) is an an edge-on view of a coupon after it had been coated with Acktar Magic Black. The inherent thickness of the coating no longer renders the edge sharp, producing a terminal radius of approximately 10-15 μm. In an attempt to retain the edge sharpness, a lower-thickness coating from Acktar was implemented and is shown in Figure 9(b). It is apparent that the terminal radius is decreased compared to the coupon with the standard thickness coating, however the edge radius is still approximately 5 μm, or roughly 10

- 20 times greater than the uncoated edge. It can also be seen that the coating tends to coalesce around the terminal edge, further reducing its sharpness. It should be noted that several other coatings on sharp amorphous metal edges were explored, however they were either incompatible with the thickness of the material, or resulted in irregular edge profiles.

3. SCATTEROMETER TESTBED

3.1 Testbed Description

A custom scatterometer was built (see Ref [10]) for characterizing the solar glint from the optical edge candidates mentioned above. The scatterometer imitates the geometry of sunlight glinting from a starshade edge into a distant telescope. For convenience the geometry is reversed so that light comes from a collimated beam normal to the face of the sample, and is collected over an aperture that subtends 32 arcmin, the angular diameter of the sun. The scatterometer separately measures the linearly polarized light, both parallel and perpendicular, to the edge scattering plane defined by the illumination-view geometry.

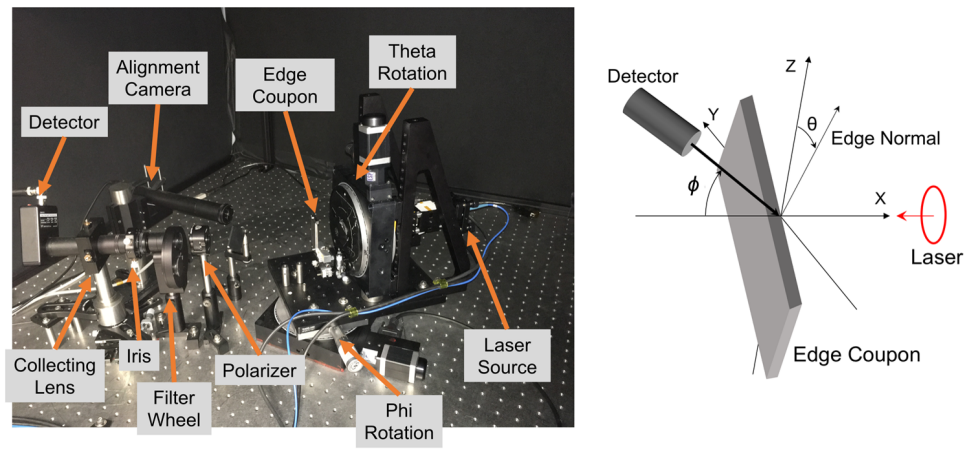

(a) (b)

Figure 10. a) Scatterometer testbed showing the two-axis stage used to rotate the edge coupon. A CCD camera is used to assist in setup and alignment and the laser source is attached to the rotation stages. The detector is in the effective optical position of the sun, while the laser is in the position of the telescope. b) A simplified schematic showing the geometry of the scatterometer as well as the two rotations ϕ and θ.

Figure 10 shows the laboratory setup and a simplified schematic illustrating the scatterometer geometry. A collimated and nominally linearly polarized source at 633 nm from a fiber-coupled laser passes through a linear polarizer to clean up any polarization rotations in the output beam, and a quarter-wave plate resulting in a circularly polarized beam. After scattering from the edge under test, the light passes through a linear polarizer into an iris, lens, and photodetector combination arranged to have a 32 arcminute field of regard. The fiber's output state of polarization changes slightly as the cable twists during a measurement, leading to power losses upon transmission through the linear polarizer. To address this problem, the light passes through a 10:90 (R:T) beamsplitter and the reflected light enters a small photodetector for power calibration.

The edge coupon, approximately 2" by 1" in size, is mounted on two orthogonal rotation stages enabling rotation through all angles of interest by computer control, and is aligned so that the edge of the coupon is centered in the detector field of view for all rotation angles. By rotating the vertical-axis stage, the angle ϕ, corresponding to the angle of the sun relative to the surface normal of the starshade, can be adjusted from -90° to + 90°. For example when $\phi = 85°$, the sun is nearly edge on to the starshade, while $\phi = 20°$ places the sun well behind the starshade where the glint angle is shallow. The horizontal axis stage adjusts the angle θ through 360°. This stage rotates the edge normal, the fiber, and associated optics around the line of sight to the telescope (or in the lab case, it is rotation about the direction to the source). This simulates the orientation of

edge segments around the perimeter of the starshade. Angle $\theta = 0°$ is the specular reflection angle and places the global normal of the edge along the z-axis in the scattering plane defined by the sun direction and the line of sight (in the laboratory, it is the plane of the collimated beam and the direction to the detector). For angles θ of - 90° through zero to 90°, light from the laser may reflect off the edge directly into the detector. We term this the "leading edge" orientation, as mentioned in Section 2. For the opposite angles, no direct reflection is possible and we term this the "trailing edge". Starshade requirements focus on the leading edge conditions because the trailing edges will be shadowed from the sun using the CFRP substrates on the sun-facing side of the starshade, as shown in Figure 3.

Scattered light from the edge coupon first passes through a linear polarizer selecting for either s- (parallel to the edge) or p- (normal to the edge) polarization and then through a 3 mm diameter iris. To increase the dynamic range of the instrument, the light also passes through an automated filter wheel containing neutral density (ND) filters ranging from open (ND 0) to ND 5. The light is then collected with a lens and is focused onto a sensitive, low noise silicon photodiode detector. To mitigate stray light, parts of the equipment were blackened, but generally, sight lines prevent stray light from entering the detector. To eliminate room light, the setup was completely encased in a black box, and a narrow band filter was mounted in front of the detector. The laser source ($\sim$ 1.5 mW) is modulated at 500 Hz and detected using a lock-in amplifier. Data from the scatterometer is acquired via an analog to digital converter.

3.2 Scaling Relations

Because the geometry of the scatterometer mimics the space geometry, conversion of the testbed data to the space case is straightforward. As shown in Ref [10], for a specular edge, the ratio of the measured scattered power in space, P_S, to that in the laboratory, P_L, for an illuminated section of edge of height, h_{eS}, is given by:

$$\frac{P_S}{P_L} \approx \frac{I_S A_S h_{eS} R_L}{I_L A_L \alpha R_S^2}, \tag{1}$$

where I denotes irradiance, A is the area of the apertures with subscripts L and S denoting laboratory and space, and R the ranges of the telescope or detector from the edge.

For an edge exhibiting Lambertian scattering properties:

$$\frac{P_S}{P_L} \approx \frac{I_S A_S h_{eS} R_L^2}{I_L A_L h_{eL} R_S^2}. \tag{2}$$

We arrange that $h_{eL}/R_L = \alpha$ so that the expressions are equivalent and then the scattered power scaling ratio is independent of the specularity and diffusivity of the surface. Using for example, $I_S = 500$ W/m^2, $I_L = 25$ W/m^2, $A_S = 1$ m^2, $A_L = 7 \times 10^{-6}$ m^2, $h_{eS} = 1$ m, $h_{eL} = 0.003$ m, $R_L = 0.3$ m, and $R_S = 48.8 \times 10^6$ m, we find that $P_S/P_L \sim 3.6 \times 10^{-8}$.

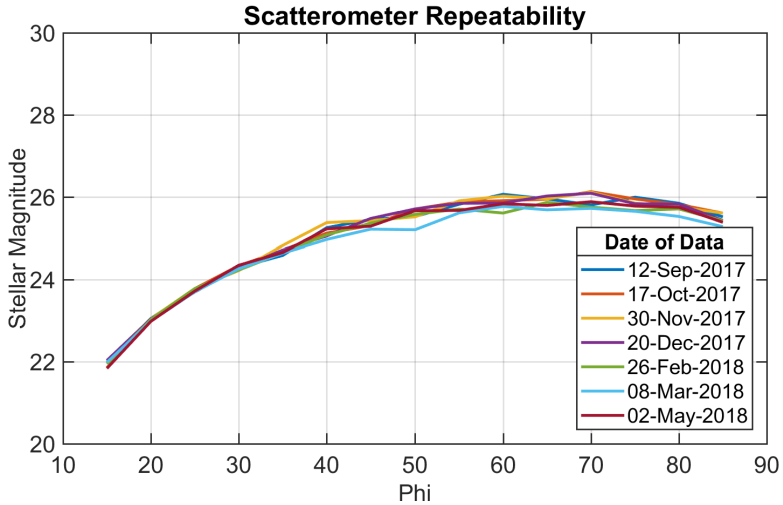

Figure 11. Scatter results, in total flux (combined s- and p-polarizations), for a standard razor blade taken over a period of approximately 7 months indicating a deviation of less than 0.5 stellar magnitudes over all sun angles.

3.3 Measurement Repeatability

To test the scatterometer stability, a standard razor blade was repeatedly measured over a period of about seven months. This method of testing is not definitive, as the razor quality can deteriorate with handling and exposure to the laboratory environment. To minimize this deterioration, the razor is kept in an enclosed holder, is carefully cleaned before each measurement, and is handled as little as possible with gloves. Figure 11 shows the scatter results of the total flux (s- and p-polarization combined) of the razor. The figure axes are ϕ, the angle of the source to the starshade normal, and the visual magnitude of the total light glinting from the telescope for a given starshade perimeter length and distance. The stability is better than $\pm$ 0.25 magnitude ($\pm$ 20%) The data shown have been averaged over angles $-90° < \theta < +90°$, which simulates the range of angles presented by the starshade perimeter.

3.4 Scattered-Light Performance

The scatterometer testbed is the primary means by which the scattered light performance of the various optical edge coupons are evaluated. Figure 12 summarizes the performance results for various optical edge candidates. It is apparent that the bare amorphous metal (AM) edges are the highest performing design with properties close to that of the GEM razor shown in Figure 11. The edges are dimmer than a 25th magnitude over all relevant sun angles (40° - 85°). It can also be seen that both the standard thickness and thin Acktar anti-reflective coatings, mentioned in Section 2.3, tend to decrease the performance of the amorphous metal edges. This is attributed to the increase in radius of the terminal edge which no longer leaves a sharp edge. Furthermore, the anti-reflection coated titanium edges display significantly worse performance than the amorphous metal edge which is again due to the relatively blunt edge. Figure 12 also displays the performance for pyrolytic graphite, an inherently dark material; however, it is approximately 1 stellar magnitude brighter in comparison to the amorphous metal edges over all sun angles. Therefore, sharp, uncoated amorphous metal edges have been chosen as the baseline design for future efforts.

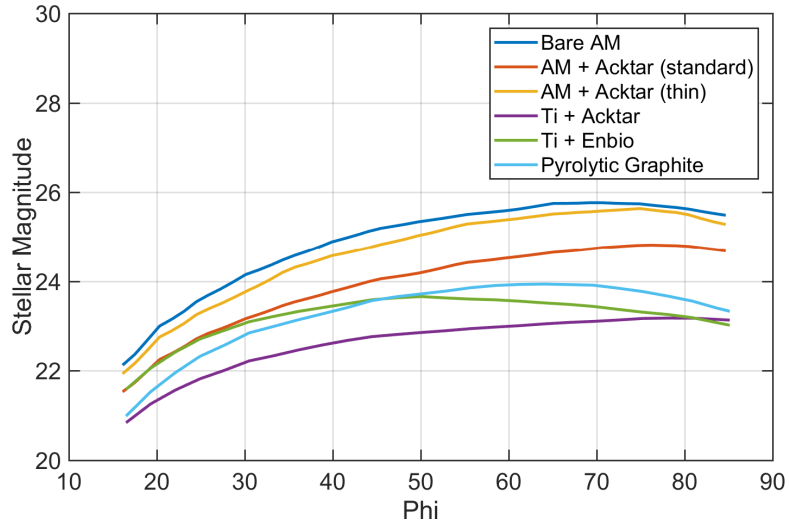

Figure 12. Scatter performance, in total flux (combined s- and p-polarizations), of optical edge coupons constructed using various materials, anti-reflective coatings, and manufacturing processes.

4. GEOMETRICAL SCATTER MODELING

4.1 Microfacet Model

In Ref [10], we represented the geometrical scatter of incident sunlight on the smooth, radiused starshade edge as a combination of two components: the specular and diffuse scattering. A small fraction of the edge exhibits the proper orientation to specularly reflect light from the sun to the telescope while the illuminated area on the edge is modeled as Lambertian for diffuse scatter. To improve upon the current state of the model, the specular and diffuse scatter can both be represented by the Microfacet model. The Microfacet model predicts the bidirectional reflectance distribution function (BRDF) for a roughened surface that is divided into mirror-like microfacets where a fraction of these facets possess the proper tilt angle to specularly reflect light into the solid angle of the telescope.[11,12] This model does not limit the specular reflection to the global geometry of the surface along the edge and predicts the off-specular scatter based on the local geometries of the microfacets.

The analytical form of the Microfacet model derived in [11] and [12] relates the BRDF to the probability density function (PDF) of the microfacet slopes. The PDF of slopes typically follow a Gaussian or Uniform distribution.[13] However, as shown in the next section, we measure the height distribution of test edges in a laser confocal microscope that may not have an analytical slope distribution representation. We instead numerically calculate the reflected power collected by the telescope using slopes computed from the measured height data.

A surface can be divided into microfacets that each have their own surface normal, $\hat{\eta}_i$, that is tilted away from the global normal at an angle, β_i. The grid used to divide the surface ensures that each microfacet shares the same projected area, dA. The effective area, $dA_i = dA/\cos\beta_i$, is defined in the plane perpendicular to the facet normal and is the area that intercepts the solar irradiance, I, on the microfacet. The incident power on the ith facet is

$$P_{in,i} = I\cos\gamma_i dA_i. \tag{3}$$

The angle of incidence on each facet is $\cos\gamma_i = \hat{\eta}_i \cdot \hat{k}_0$ where $\hat{k}_0$ is the incident sunlight direction. Each facet possesses a unique surface normal that defines the local s- and p- polarization directions. We employ Polarization Ray Tracing (PRT) matrices,[14] $\mathbf{P}_i$, that map global coordinates to local coordinates of each facet, apply Fresnel reflection for a material with complex index of refraction n, and map back to global coordinates for incident E-fields, $\vec{E}_{in,i} = \sqrt{P_{in,i}}\hat{E}_{in}$. The PRT matrices track the polarization and reflection effects for each facet. The current model takes into account a single interaction with each facet. However, the model can be easily extended

to account for multiple interactions of light with the microfacets with the aid of PRT matrices. If the polarization of the incident E-field is aligned with s- or p- polarization directions of the facet, the matrix multiplication scales the E-field amplitude by the Fresnel reflection coefficient, $r_{s,p}$. Note that more light will be reflected for larger incident angles based on Fresnel reflection coefficient equations. The output E-field after interacting with the facet is $\vec{E}_{out,i} = \sqrt{P_{in,i}}\mathbf{P}_i\hat{E}_{in}$ and thus the reflected power is

$$P_{out,i} = I\cos\gamma_i dA_i \langle \mathbf{P}_i\hat{E}_{in}|\mathbf{P}_i\hat{E}_{in}\rangle = \rho_i I\cos\gamma_i dA_i, \tag{4}$$

where ρ_i is the reflectivity of the facet for the incident E-field.

The total reflected power that is collected depends on the view direction and solid angle of the telescope. The reflected direction is found for each facet and checked if within the solid angle of the telescope, Ω_T. The number of facets that contribute to the power for the illumination-view geometry with scattering angle, Φ, and collected by the telescope is $n(\Phi, \Omega_T)$. The total power is then the sum of the power from each contributing facet for a particular sun-telescope geometry. For the single reflection case, the contributing facets will exhibit similar power due to the small telescope solid angle. The total reflected power for the length of edge is

$$P_{out} = n(\Phi, \Omega_T)\rho I\cos\left(\frac{\Phi}{2}\right)\frac{dA}{\cos\beta}, \tag{5}$$

where half the scattering angle is equal to the angle of incidence on the facet and β is the tilt angle for specular reflection. The total power is directly related to the number of facets collected by the telescope for an illumination-view geometry. In our previous work, we represented the edge as a thin sheet comprised of an angled side that meets the face of the starshade with a radiused corner.[10] In the present work, an increase of the radius results in an increase in the surface area and the number of facets of the edge. More facets will contribute to the reflected power collected by the telescope; larger edge radius results in a brighter edge due to an increase in $n(\Phi, \Omega_T)$.

This represents the reflected power from a small sampled section of length, l_{sample}, of the test edge and can be scaled to the total length of the starshade edge, l, with N petals. Also, the sunlight reflected from each facet spreads into an area due to the angular subtense of the sun, α, such that only a fraction of the reflected light is collected by the telescope with area, A, at the distance, R, from the starshade,

$$P_{out} = \frac{Nl}{l_{\text{sample}}}\frac{A}{\pi/4(\alpha R)^2}n(\Phi, \Omega_T)\rho I\cos\left(\frac{\Phi}{2}\right)\frac{dA}{\cos\beta}. \tag{6}$$

4.2 Edge Characterization

Accurate modeling of the optical characteristics of a sample coupon requires an understanding of the physical geometry of the edge on a sub-micron level. Our model utilizes a 3-dimensional reconstruction of the terminal edge which breaks the edge down into thousands of microfacets.

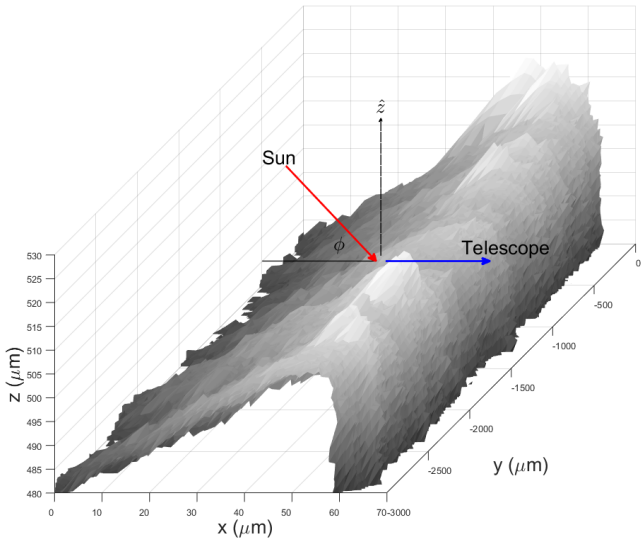

Figure 13. Pyrolytic graphite edge measured in the laser confocal microscope and imported into the microfacet model. The red arrow represents the solar illumination direction at angle, ϕ, from the x-axis (the surface normal of the starshade face) and the blue arrow represents the telescope view direction for the space case. The laboratory and simulation cases reverse the illumination and view directions. Direction of arrows indicate photon travel.

There are several ways to obtain suitable 3D models. One such method is with the use of a laser scanning confocal microscope. The microscope is able to scan a surface and collect both an optical image and high-resolution surface data. Nanometer-level heights can be measured by analyzing the intensity of the returned laser light relative to the z-position of the laser. The accompanying software then creates a heightmap of the edge which can be used in the optical model. Figure 13 shows a typical heightmap of a machined pyrolytic graphite edge coupon that has been imported into the optical model.

This method has worked well on relatively blunt edges with a radius of curvature on the order of ~ 10 μm, but has not yet been successful at scanning sharper (RoC < 1 μm) edges. Another method which has seen some success on these small scales is the use of optical photogrammetry software with SEM images.[15] Optical photogrammetry uses a large number of overlapping images to reconstruct a 3D model of a target. With the relatively simple geometry of the optical edges, there will not be any structures left out of the reconstruction, such as can happen with complicated or concave targets. However, a lack of suitable identifiable points on the surface of the coupon may result in a poorly reconstructed model. We are currently investigating this approach.

4.3 Preliminary Model Results

Light scattered from the edges of test blades are measured in the scatterometer testbed described in Section 3. The scatterometer sweeps the detector over angle, ϕ, to scan the amount of scattered light for a stationary illumination direction that is normal to the sample face. For convenience, we employ reciprocity between the solar illumination and telescope directions for the numerical microfacet model calculation; the sun will change its illumination direction in space while the telescope view direction is stationary. Figure 13 shows the illumination-view geometry. The illumination direction is represented as the red arrow measured from the x-axis (the surface normal of the face of the starshade) by angle, ϕ, and the telescope view direction in blue. The microfacet model simulation mimics the measurement sequence of the scatterometer by finding the amount of reflected power for two orthogonal polarization orientations at each angle of ϕ for different rotational orientations, θ, of the blade. Like the scatterometer, the incident E-field in the microfacet model is circularly polarized. During the measurement sequence, the illumination and telescope view geometry remain in the xz-plane (known as the scattering plane) such that we can calculate the amount of reflected s- and p- polarized light. The s- and p-polarized light represents orientations that are perpendicular and parallel, respectively, to the scattering plane.

Figure 14 compares the simulated to measured reflected power in stellar magnitudes for s- and p-polarization orientations for the pyrolytic graphite sample shown in Figure 13. The model for s-polarization is in good agreement with the data over the range $30° < \phi < 85°$. (Note that observations with the HABEX starshade concept will be restricted to $40° < \phi < 85°$). At lower angles, where diffraction is expected to be the dominant source of light, the models predict less light than is observed in the scatterometer. This is likely due to our diffraction formulation which treats the edge as infinitesimally thin. Diffraction around the curved edge (radius of curvature $\sim 10\ \mu m$) will have a somewhat different character. This is presently being explored through Finite Difference Time Domain analyses. In the p-polarization, the model predicts ~ 1 magnitude ($2.5\ \times$) less scatter than is observed. One possible explanation is leakage of s-polarized light into the p-polarization. This would explain both the slight overestimate of s and underestimate of p by the model. Further analysis is underway to improve upon the current state of the model.

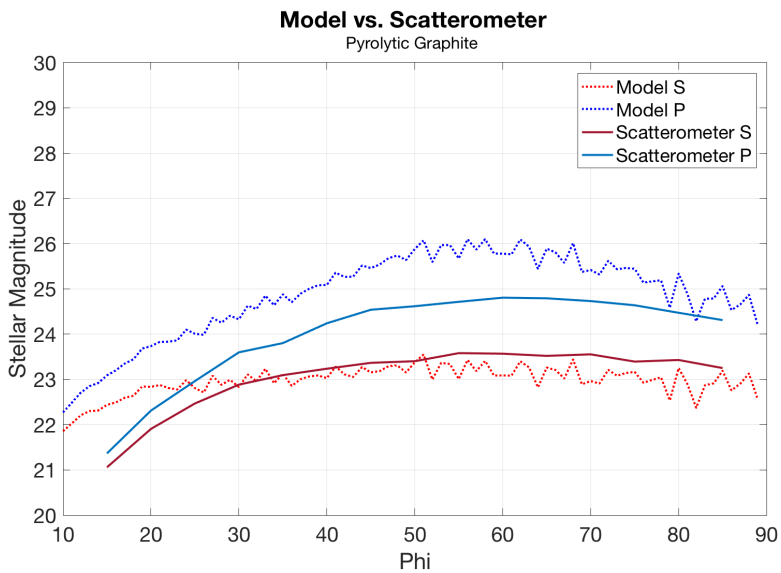

Figure 14. Data measured in the scatterometer of the pyrolytic graphite edge compared to the numerical microfacet model.

5. STEALTH EDGES

Our work to date indicates that specular, sharp edges are superior to low-reflective blunt edges such as those studied in Ref [9]. With smooth, sharp edges, the glint is concentrated in a few small edge sections around the starshade perimeter where the specular reflection and diffraction are dominant (Figure 15). When viewed by the telescope, which only resolves the distant starshade with a resolution of a few pixels, the glint appears as shown in Figure 16(a). A solution to reducing this glint is to replace the bright portions of these glinting edges with a serrated edge having a period of 1 - 2 mm and amplitude of 0.2 - 0.5 mm, as shown in Figure 16(b). Much like the stealth edges around the cockpit, fuselage, and engines of a stealth fighter jet, the serrated edges direct the sunlight away from the telescope. The period and amplitude are small enough that the diffraction of the starlight and subsequent depth of the shadow are unaffected. Thus starlight remains suppressed while sunlight glint is greatly reduced. In the example shown in Figure 16(b), approximately 3 m of the 384 m edge are populated with the "stealth" edges. The reflected solar glint is reduced by more than 2 visual magnitudes. Through optimization of the shape of the serrated edges, the glints can be reduced by an additional order of magnitude.

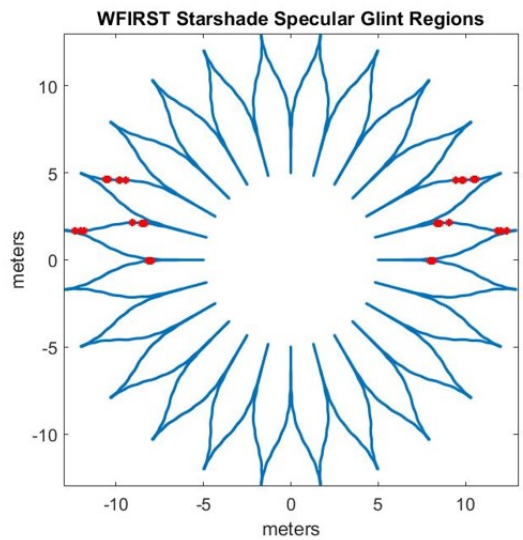

Figure 15. Assuming that the sun is behind the starshade and along the vertical axis (x = 0), the red points show the regions oriented for specular reflection into the telescope. These are the regions that are replaced with serrated edges.

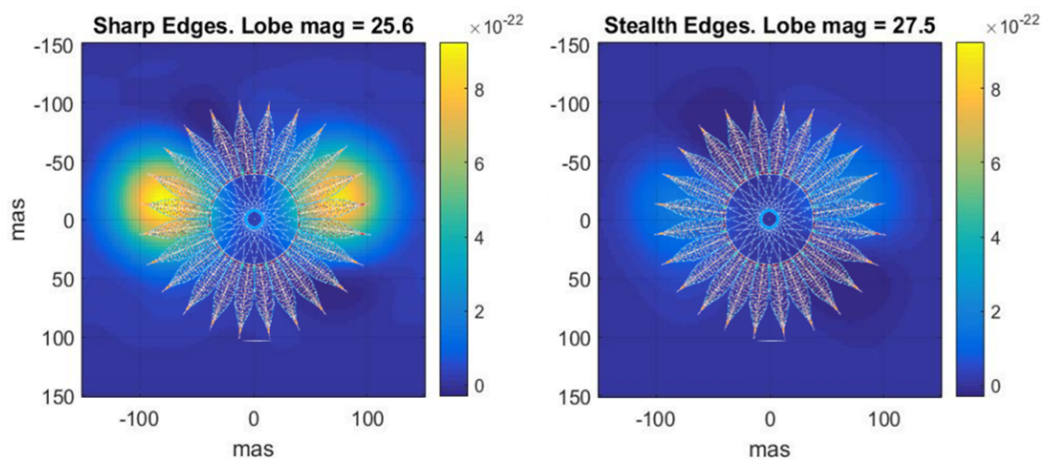

(a) (b)

Figure 16. WFIRST starshade, diameter 26 m, distance 26 Mm, wavelength 760 nm, Sun angle 60 deg from normal. a) The glint concentrates into two lobes as seen by the telescope. Each lobe is equivalent to a star with visual magnitude $\sim$ 25.6, depending on the wavelength and the distance to the starshade. A skeleton starshade is shown for scale. b) When the specular edge segments are replaced with a serrated edge, the scatter is greatly reduced. Laboratory scatter data of a straight edge and a serrated edge etched from amorphous metal were used to generate the solar glint images.

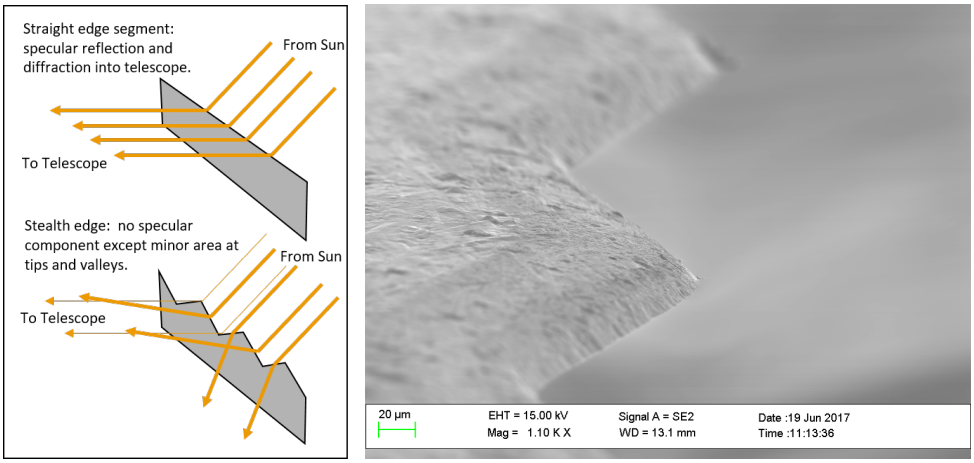

(a) (b)

Figure 17. a) Depiction of specular reflection (top) and stealth edge concept (bottom). Only the tips and valleys present a specular component that glints into the telescope. b) SEM image of an amorphous metal stealth edge coupon.

6. CONCLUSIONS

This paper provided an overview of the technical efforts performed to date to develop precision low-scatter optical edges for future starshades. While a significant amount of work remains to incorporate these optical edges into a full-scale system, progress has been made towards meeting performance requirements for future exoplanet detecting missions. The major findings of this effort are as follows:

- Etched amorphous metal edges are capable of meeting requirements related to in-plane dimensional accuracy and solar scatter for future starshade missions.
- Anti-reflective coatings are unable to meet scattered-light performance requirements due to the increase in terminal radius produced as a result of their finite thickness.
- Geometrical scatter models are under development to predict the magnitude of reflected and/or diffracted light from various edge profiles.
- "Stealth Edges" can eliminate the scattered light emanating from areas on the starshade where specular reflection and diffraction are dominant.

ACKNOWLEDGMENTS

A decision to implement a starshade flight mission or the other future space telescope concepts described above will not be finalized until NASAs completion of the National Environmental Policy Act (NEPA) process. This document is being made available for information purposes only. This research was carried out at the Jet Propulsion Laboratory, California Institute of Technology under a contract with the National Aeronautics and Space Administration (NASA). © 2018 California Institute of Technology. Government sponsorship acknowledged.

REFERENCES

1. Kouveliotou, C., Agol, E., Batalha, N., Bean, J., Bentz, M., Cornish, N., Dressler, A., Figueroa-Feliciano, E., Gaudi, S., Guyon, O., et al., "Enduring quests-daring visions (nasa astrophysics in the next three decades)," *arXiv preprint arXiv:1401.3741* (2014).
2. Mennesson, B., Gaudi, S., Seager, S., Cahoy, K., Domagal-Goldman, S., Feinberg, L., Guyon, O., Kasdin, J., Marois, C., Mawet, D., et al., "The habitable exoplanet (habex) imaging mission: preliminary science drivers and technical requirements," in [*Space Telescopes and Instrumentation 2016: Optical, Infrared, and Millimeter Wave*], **9904**, 99040L, International Society for Optics and Photonics (2016).

3. Seager, S., Kasdin, J., and Team, S. R. P., "Starshade rendezvous mission probe concept," in [*American Astronomical Society Meeting Abstracts*], **231** (2018).
4. Seager, S., Turnbull, M., Sparks, W., Thomson, M., Shaklan, S. B., Roberge, A., Kuchner, M., Kasdin, N. J., Domagal-Goldman, S., Cash, W., et al., "The exo-s probe class starshade mission," in [*Techniques and Instrumentation for Detection of Exoplanets VII*], **9605**, 96050W, International Society for Optics and Photonics (2015).
5. Shaklan, S. B., Marchen, L., and Cady, E., "Shape accuracy requirements on starshades for large and small apertures," in [*Techniques and Instrumentation for Detection of Exoplanets VIII*], **10400**, 104001T, International Society for Optics and Photonics (2017).
6. Webb, D., Hirsch, B., Bradford, C., Steeves, J., Lisman, D., Shaklan, S., Bach, V., and Thomson, M., "Advances in starshade technology readiness for an exoplanet characterizing science mission in the 2020's," in [*Advances in Optical and Mechanical Technologies for Telescopes and Instrumentation II*], **9912**, 99126H, International Society for Optics and Photonics (2016).
7. Arya, M., Webb, D., McGown, J., Lisman, P. D., Shaklan, S., Bradford, S. C., Steeves, J., Hilgemann, E., Trease, B., Thomson, M., et al., "Starshade mechanical design for the habitable exoplanet imaging mission concept (habex)," in [*Techniques and Instrumentation for Detection of Exoplanets VIII*], **10400**, 104001C, International Society for Optics and Photonics (2017).
8. Steeves, J., Martin, S., Webb, D., Lisman, D., and Shaklan, S., "Precision optical edges for a starshade external occulter," in [*Advances in Optical and Mechanical Technologies for Telescopes and Instrumentation II*], **9912**, 99122O, International Society for Optics and Photonics (2016).
9. Casement, S., Warwick, S., Smith, D., Ellis, S., and Stover, J., "Results of edge scatter testing for a starshade mission," in [*Space Telescopes and Instrumentation 2016: Optical, Infrared, and Millimeter Wave*], **9904**, 99043H, International Society for Optics and Photonics (2016).
10. Martin, S. R., Shaklan, S., Crawford, S., Lee, S.-C., Khayatian, B., Hoppe, D., Cady, E., and Lisman, P. D., "Starshade optical edge modeling, requirements, and laboratory tests," in [*Techniques and Instrumentation for Detection of Exoplanets VI*], **8864**, 88641A, International Society for Optics and Photonics (2013).
11. K. E. Torrance and E. M. Sparrow, "Theory for Off-Specular Reflection From Roughened Surfaces," *Journal of the Optical Society of America* **57**(9), 1105–1114 (1967).
12. Priest, R. G. and Meier, S. R., "Polarimetric microfacet scattering theory with applications to absorptive and reflective surfaces," *Optical Engineering* **41**(5), 988 (2002).
13. Cox, C. and Munk, W., "Measurement of the Roughness of the Sea Surface from Photographs of the Sun's Glitter," *Journal of the Optical Society of America* **44**(11), 838 (1954).
14. Yun, G., Crabtree, K., and Chipman, R. A., "Three-dimensional polarization ray-tracing calculus i: definition and diattenuation," *Appl. Opt.* **50**, 2855–2865 (Jun 2011).
15. Eulitz, M. and Reiss, G., "3d reconstruction of sem images by use of optical photogrammetry software," *Journal of structural biology* **191**(2), 190–196 (2015).